Understanding the Relationships between Lightning, Cloud Microphysics, and Airborne Radar-Derived Storm Structure during Hurricane Karl (2010)

BRAD REINHART,* HENRY FUELBERG,* RICHARD BLAKESLEE,+ DOUGLAS MACH,#
ANDREW HEYMSFIELD,@ AARON BANSEMER,@ STEPHEN L. DURDEN,& SIMONE TANELLI,&
GERALD HEYMSFIELD,** AND BJORN LAMBRIGTSEN&

* *The Florida State University, Tallahassee, Florida*
+ *NASA Marshall Space Flight Center, Huntsville, Alabama*
# *Earth System Science Center, University of Alabama in Huntsville, Huntsville, Alabama*
@ *National Center for Atmospheric Research, Boulder, Colorado*
& *Jet Propulsion Laboratory, California Institute of Technology, Pasadena, California*
** *NASA Goddard Space Flight Center, Greenbelt, Maryland*

(Manuscript received 26 December 2012, in final form 2 August 2013)

ABSTRACT

This study explores relationships between lightning, cloud microphysics, and tropical cyclone (TC) storm structure in Hurricane Karl (16 September 2010) using data collected by the NASA DC-8 and Global Hawk (GH) aircraft during NASA's Genesis and Rapid Intensification Processes (GRIP) experiment. The research capitalizes on the unique opportunity provided by GRIP to synthesize multiple datasets from two aircraft and analyze the microphysical and kinematic properties of an electrified TC. Five coordinated flight legs through Karl by the DC-8 and GH are investigated, focusing on the inner-core region (within 50 km of the storm center) where the lightning was concentrated and the aircraft were well coordinated. GRIP datasets are used to compare properties of electrified and nonelectrified inner-core regions that are related to the noninductive charging mechanism, which is widely accepted to explain the observed electric fields within thunderstorms. Three common characteristics of Karl's electrified regions are identified: 1) strong updrafts of 10–20 m s^{-1}, 2) deep mixed-phase layers indicated by reflectivities >30 dBZ extending several kilometers above the freezing level, and 3) microphysical environments consisting of graupel, very small ice particles, and the inferred presence of supercooled water. These characteristics describe an environment favorable for in situ noninductive charging and, hence, TC electrification. The electrified regions in Karl's inner core are attributable to a microphysical environment that was conducive to electrification because of occasional, strong convective updrafts in the eyewall.

1. Introduction

The sporadic nature of lightning in tropical cyclones (TCs) remains a topic of great interest to the research community. Because TCs frequently develop over distant tropical oceans, the availability of continuous storm data often is limited. While satellites have greatly improved our ability to monitor TCs in real time, inner-core and other TC structural changes are not always evident from satellite imagery alone. In recent years, lightning detection networks have been providing real-time, continuous information about electrical activity within TCs around the world. These valuable datasets afford researchers the opportunity to more thoroughly examine TC electrification.

Lightning occurs less frequently in TCs and oceanic convection than in continental convective systems (Cecil et al. 2002; Williams and Stanfill 2002). The noninductive charging mechanism that is believed to be the major process leading to storm electrification requires collisions between graupel and ice particles in the presence of supercooled water (e.g., Takahashi 1978; Saunders and Peck 1998; Saunders 2008; Emersic and Saunders 2010). A deep mixed-phase region (commonly defined as the 0° to −20°C layer) provides the necessary environment where collisions between ice particles separate charge and produce storm electrification. Since TC

Corresponding author address: Henry Fuelberg, Department of Earth, Ocean, and Atmospheric Science, The Florida State University, 1017 Academic Way, Tallahassee, FL 32306-4520.
E-mail: hfuelberg@fsu.edu

DOI: 10.1175/MWR-D-13-00008.1

updrafts generally are weaker than those of continental convection (Jorgensen et al. 1985; Jorgensen and LeMone 1989; Black et al. 1996), the smaller frequency of lightning in TCs may be attributed to an insufficient amount, or vertical depth, of supercooled water and graupel particles necessary for noninductive charging.

Similar to garden-variety thunderstorms, charge separation in the eyewall of a TC greatly depends on the relative amounts of supercooled water, graupel, and ice crystals within its updrafts (Black and Hallett 1999). Supercooled water above the −5°C level in TCs is rare since the efficient radial and azimuthal advection of ice particles produced by eyewall convection reduces the amount of supercooled water available in TC updrafts (Black and Hallett 1986; Marks and Houze 1987; Houze et al. 1992). Although rare in TCs, the presence of supercooled water well above the freezing level has been inferred in those TCs having strong vertical motions (Herman and Heymsfield 2003; Black et al. 2003; Heymsfield et al. 2009). TC updrafts of sufficient magnitude ($>10\,m\,s^{-1}$; Black and Hallett 1999), though uncommon, have been observed in intense and/or rapidly intensifying TCs (Black et al. 1994; Black and Hallett 1999; Cecil et al. 2010; Guimond et al. 2010; Heymsfield et al. 2010). The precipitation associated with strong TC updrafts cleanses the air of aerosols that can serve as ice nuclei for ascending droplets in the updraft. This lack of ice nuclei allows supercooled droplets to exist in the strong updrafts at much colder temperatures before the droplets freeze homogeneously (Black et al. 2003). Therefore, strong updrafts ($>10\,m\,s^{-1}$) that can support a deep mixed-phase layer containing abundant supercooled water are most conducive to TC electrification (Black and Hallett 1999).

The characteristics of electrified TCs and oceanic convection have been analyzed using various remote-sensing techniques. Vertical profiles of radar reflectivity have been used to assess the microphysical structure and the potential for lightning activity within oceanic convection. Enhanced reflectivity within the mixed-phase region represents an increase in droplet, graupel, and ice particle size and/or concentration (Petersen et al. 1996, 1999). Radar reflectivity in TCs and tropical oceanic convection generally decreases rapidly above the freezing level (Jorgensen et al. 1985; Szoke et al. 1986; Marks and Houze 1987; Zipser and Lutz 1994; Black et al. 1996; Rogers et al. 2007; Heymsfield et al. 2010). Thus, lightning probability (Cecil and Zipser 2002) and flash rates (Petersen et al. 1996, 1999) increase with increasing reflectivity throughout the troposphere, especially within the mixed-phase region. Microwave ice scattering signatures also have been used to identify regions where precipitation-sized ice is present. Lightning is more likely to occur in regions with decreased 85- and 37-GHz brightness temperatures due to increased ice scattering (Cecil and Zipser 2002; Cecil et al. 2010).

The spatial and temporal variations of TC lightning have been well documented in recent years. Molinari et al. (1994, 1999) found a distinct radial pattern of lightning in Atlantic hurricanes: a weak maximum in the eyewall, a clear minimum in the region outside the eyewall, and a strong maximum in the outer rainbands. In the idealized TC modeled by Fierro et al. (2007), the greatest total lightning [cloud to ground (CG) and intracloud (IC)] flash rates occurred in the eyewall, where stronger updrafts produced a favorable charging environment. Many recent TC lightning studies (including but not limited to Lyons and Keen 1994; Samsury and Orville 1994; Molinari et al. 1994, 1999; Shao et al. 2005; Squires and Businger 2008; Price et al. 2009; Austin and Fuelberg 2010; Cecil et al. 2010; Demetriades et al. 2010b; DeMaria et al. 2011; Fierro et al. 2011) have examined relationships between TC electrification and changes in storm intensity. The results of these studies have been mixed. Further examining the tenuous link between lightning frequency and TC intensity is not the objective of our present research.

Our study focuses on the physical properties that contributed to the electrification of Hurricane Karl (2010). We explore relationships between lightning, cloud microphysics, and TC storm structure using data gathered from research flights into Hurricane Karl on 16 September 2010. Although previous observational studies (e.g., Black and Hallett 1999; Cecil et al. 2002; Cecil and Zipser 2002; Cecil et al. 2010) have analyzed characteristics of electrified TCs, our study synthesizes an unprecedented number of in situ datasets collected within Karl during the National Aeronautics and Space Administration's (NASA) 2010 Genesis and Rapid Intensification Processes (GRIP) experiment (Braun et al. 2013). Coordinated flight legs by the DC-8 and Global Hawk (GH) aircraft are classified based on observed lightning activity. GRIP datasets are used to analyze each coordinated flight leg through Karl. We then compare the microphysical and kinematic properties of electrified and nonelectrified flight legs to understand the lightning variability observed within Karl.

2. Data and methods

a. GRIP datasets

Meteorological data used in this study were collected by the NASA DC-8 aircraft and the Global Hawk Unmanned Airborne System during the 2010 NASA GRIP experiment (Braun et al. 2013). The field campaign sought to better understand how TCs form and develop

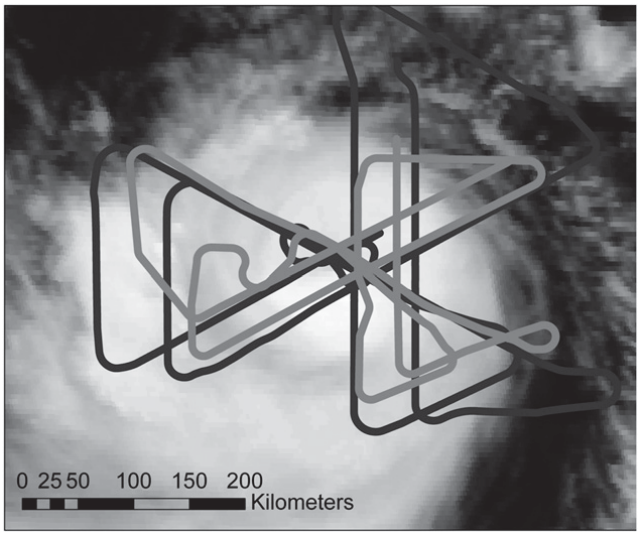

FIG. 1. Flight tracks of the DC-8 (dark gray) and GH (light gray) between 1900 and 2300 UTC 16 Sep 2010 overlaid on 2145 UTC GOES infrared satellite imagery of Hurricane Karl.

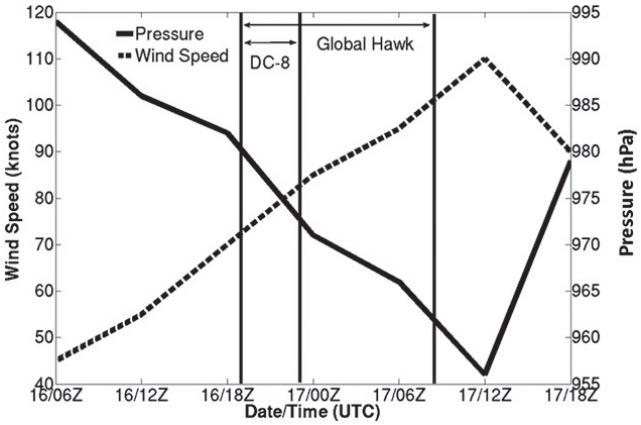

FIG. 2. Minimum central pressure (solid) and maximum sustained winds (dashed) of Karl during its rapid intensification on 16–17 Sep 2010. Sampling periods of the DC-8 and GH are superimposed for reference.

into major hurricanes by sampling storms using multiple research aircraft. At approximately 0600 UTC 16 September, Tropical Storm Karl moved off the Yucatan Peninsula and shortly thereafter began rapidly strengthening over the southwestern Gulf of Mexico. The DC-8 and GH conducted coordinated flight legs into Hurricane Karl on 16 September from approximately 1900 to 2300 UTC (Fig. 1). This observation period captured part of Karl's rapid intensification on 16–17 September from a 55-kt ($1\,\text{kt} = 0.5144\,\text{m s}^{-1}$) tropical storm to a 956-hPa, 110-kt category three hurricane (Fig. 2). During these coordinated flight legs, the DC-8 aircraft penetrated Karl at altitudes between 10.3 and 11.3 km, corresponding to flight-level temperatures of −32.2° to −45.4°C. The GH aircraft overflew the DC-8 and sampled the storm from altitudes of 17.5–18.3 km.

We synthesized several GRIP datasets to analyze the electrification of Karl during this rapid intensification period (Table 1). Ku-band (13.4 GHz) and Ka-band (35.6 GHz) reflectivities and Doppler velocities were collected aboard the DC-8 aircraft by the dual-frequency Airborne Precipitation Radar (APR-2; Sadowy et al. 2003). The Meteorological Measurement System (MMS) on the DC-8 provided flight-level temperature and wind data (Chan et al. 1998). The various microphysics probes on the DC-8 measured size distributions and concentrations of large and small particles (Baumgardner et al. 2001). Specifically, the Cloud Droplet Probe (CDP) sampled particles from 2.5 to 51 μm, while the Cloud and Aerosol Spectrometer (CAS) measured particles between 0.58 and 52.5 μm. The Precipitation Imaging Probe (PIP) provided two-dimensional images of larger particles in a 64-element array with 100 μm per pixel resolution for additional microphysics analysis. No measurements of supercooled water were made on the 16 September flight, which is expected given that the flight-level temperatures were between −32° and −45°C. However, the microphysical datasets will be used later to infer the presence of supercooled water below the aircraft.

The Lightning Instrument Package (LIP) aboard the GH aircraft consisted of electric field mills that sampled the three-dimensional components of the electric field, thereby providing in situ information about total (CG and IC) lightning within the storm (Mach et al. 2009; Blakeslee et al. 2014). Lightning flashes were inferred from abrupt changes in the electric field near the aircraft. LIP has a fairly short range of detection, although it varies based on the field environment near the instrument. Weak electrical activity along the flight path allows LIP to detect strong flashes that are several tens of kilometers away from the aircraft. Previous campaigns (e.g., Mach et al. 2009) have revealed that LIP has a small false detection rate. Brightness temperatures from the High-Altitude Monolithic Microwave Integrated Circuit (MMIC) Sounding Radiometer (HAMSR) (Brown et al. 2011) aboard the GH were used to identify regions of deep convection and assess how well these regions were sampled by the aircraft. Reflectivity data from the High-Altitude Imaging Wind and Rain Airborne Profiler (HIWRAP; Li et al. 2011) on the GH also provided valuable information about Karl's vertical structure.

b. *Additional lightning datasets*

The LIP-derived lightning data were supplemented by information from two ground-based lightning networks

TABLE 1. GRIP datasets used in this study. Additional information for each instrument is contained in the text.

GRIP instrument	Aircraft	Data used
APR-2	DC-8	Ku- and Ka-band reflectivities and Doppler velocities; microphysics classification product
Cloud microphysics probes (CDP, CAS, PIP)	DC-8	Size distributions and total concentrations of small and large particles (0.58–6400 μm)
HIWRAP	GH	Ku-band reflectivity data
HAMSR	GH	50.30-/113.25-GHz brightness temperatures
LIP	GH	Electric field measurements and total (CG and IC) lightning
MMS	DC-8	Flight-level temperature and wind data

that primarily detect CG flashes—the Vaisala Global Lightning Dataset (GLD360; Demetriades et al. 2010a) and the World Wide Lightning Location Network (WWLLN; Rodger et al. 2006). GLD360 is a relatively new lightning network, and recent validations revealed that the network's CG detection efficiency over the continental United States ranged from 86% to 92% with a location accuracy of 10.8 km (Demetriades et al. 2010a). However, the GLD360 detection efficiency was less than optimal during GRIP because of issues with the processing algorithm and sensor reliability (K. Cummins 2012, personal communication). The efficiency also is expected to be smaller over the southwest Gulf of Mexico than the continental United States. Although no GLD360 evaluation studies have been focused in our study region, other performance studies have been conducted in other parts of the world (e.g., Naccarato et al. 2010; Poelman et al. 2013).

WWLLN is a global network consisting of approximately 60 stations that detect very low frequency (VLF) radiation, or sferics, emitted by lightning discharges. WWLLN detects stronger sferics with greater efficiency, and thus, the network is most sensitive to CG lightning. There were 55 active WWLLN receiving stations during the study period (September 2010). WWLLN had a CG lightning detection efficiency of approximately 11% with an estimated location accuracy <5 km in the southwestern Gulf of Mexico during Karl (Hutchins et al. 2012; R. Holzworth 2013, personal communication). Although WWLLN has a relatively low detection efficiency (Rodger et al. 2006), recent research has noted improvement (Abarca et al. 2010) and shown that WWLLN sufficiently samples electrical activity in Atlantic TCs for many research purposes (Abarca et al. 2011). GLD360 and WWLLN lightning data were beneficial to our research because both detect lightning continuously around the world, whereas LIP only detects electrical activity within a few tens of kilometers of the GH aircraft during storm sampling.

c. *Flight leg lightning analysis*

We chose Karl for this study because intermittent periods of frequent inner-core lightning were detected by the global networks during the coordinated DC-8 and GH GRIP flights on 16 September. Five individual DC-8 and GH flight legs, approximately 20 min in duration, were subjectively defined as coordinated, straight line passes through Karl (Table 2). These legs were limited to relatively straight passes because some data quality was diminished when the plane turned or rolled. Also, there was limited coordination between aircraft when maneuvering in the outer regions of the storm to set up for the next pass.

We used LIP, GLD360, and WWLLN lightning data to examine the location and frequency of lightning along each flight leg. The shortest distance between each GLD360 and WWLLN flash and each aircraft track was calculated. Flashes that occurred during the flight legs and within 10 km of the aircraft were identified. This 10-km threshold was chosen after several different distances were evaluated. Based on our combined analyses of GRIP and lightning datasets, we are confident that data collected within 10 km of a lightning flash represent the electrified environment that produced the flash. Additionally, 10 km was within the estimated flash detection range of the LIP sensors. The flash time was compared with the time the aircraft was closest to the flash location to determine whether the lightning occurred before, during, or after data were collected in that region of the storm. This information provided a starting point for classifying each leg based on observed electrical activity.

Inner-core flashes were counted separately for the DC-8 and GH aircraft because the spatial and temporal coordination between the aircraft varied for each leg.

TABLE 2. Specifications of flight legs for GRIP flights into Hurricane Karl on 16 Sep 2010 and the lightning classification of these legs through Karl's inner core.

Leg	Start time (UTC)	End time (UTC)	Direction	Lightning classification
1	1900	1920	N–S	Nonelectrified
2	1940	2000	SE–NW	Electrified
3	2020	2045	SW–NE	Electrified
4	2110	2130	N–S	Electrified
5	2145	2205	SE–NW	Nonelectrified

We defined the inner core as the region within 50 km of Karl's center. This distinction is consistent with previous studies (Molinari et al. 1994, 1999) that designated eyewall flashes as those occurring within 40 km of storm center. We focused on the inner core because the GRIP aircraft typically were closest to each other as they penetrated Karl's eye. This coordination enabled us to use datasets from both aircraft to better evaluate the physical properties and electrical nature of Karl.

Although LIP did not provide exact two-dimensional locations of lightning, electric field vectors from LIP could be used to determine where electrical activity was occurring relative to the GH aircraft. The strength and orientation of the field vectors were plotted to assess the relative distance of charge centers from the GH flight path. The LIP data were used in conjunction with the ground-based lightning networks to subjectively classify each flight leg as either electrified or nonelectrified. Electrified legs were defined as those along which inner-core lightning activity was detected by at least one of the available lightning networks during aircraft sampling. On the other hand, a leg was classified as nonelectrified when electric fields were too weak to initiate detectable lightning activity within the sampled region. Table 2 classifies each of Karl's five flight legs. It should be emphasized that our distinction between electrified and nonelectrified flight legs strictly pertains to the presence or absence of detectable lightning along flight tracks within Karl's inner core. Figure 3 illustrates examples of an electrified (top panel) and nonelectrified (bottom panel) leg.

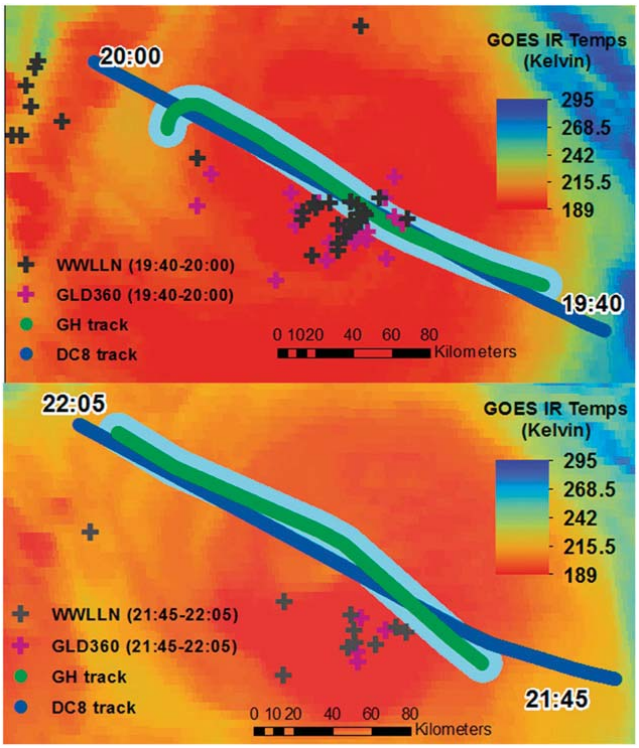

FIG. 3. (top) Electrified leg 2 and (bottom) nonelectrified leg 5 through Karl. The blue and green lines indicate the tracks of the DC-8 and GH, respectively. The light blue region highlights those lightning flashes within 10 km of the GH. Note the numerous flashes that occur near the aircraft on leg 2 and the displacement of the lightning and deepest convection from the flight tracks on leg 5.

3. Results

We first contrast the vertical motions, microphysical properties, and radar reflectivities of Karl's electrified and nonelectrified flight legs to characterize the conditions that support TC electrification. The physical parameters that we examine were sampled by the GRIP aircraft and are related to lightning production via the noninductive charging mechanism. This is followed by a detailed examination of electrified leg 2.

a. Characteristics of electrified and nonelectrified regions

1) VERTICAL VELOCITY

Noninductive charging requires strong updrafts that can support a deep mixed-phase precipitation region where charge separation can occur (e.g., Black and Hallett 1999). We used MMS flight-level vertical velocity measurements and APR-2 Doppler velocities from the DC-8 aircraft to evaluate vertical motions along each flight leg (Table 2). The DC-8 penetrated Karl at an average altitude of 10.3 km on legs 1 and 2 and 11.3 km on legs 3–5.

Figure 4 shows the distribution of DC-8 flight-level, inner-core vertical velocities categorized by the leg and the inner-core quadrant that was sampled. The majority of vertical velocities are between -2 and 2 m s^{-1}, consistent with previous findings (Jorgensen et al. 1985; Black et al. 1996; Rogers et al. 2007) that TC updrafts tend to be weak compared to convective updrafts over land. Although the majority of inner-core vertical velocities are weak, the electrified regions of legs 2 and 4 exhibit much stronger peak updrafts (20.2 and 12.5 m s^{-1}, respectively). These areas comprise a relatively small portion of the inner core; only 3.4% of the analyzed inner-core updrafts in Karl exceed 5 m s^{-1}, and less than 1% exceed 10 m s^{-1}. Conversely, the nonelectrified legs almost exclusively contain updrafts less than 6 m s^{-1}, with the southeast quadrant of leg 5 being the only exception. Leg 3 is the only electrified leg that does not exhibit strong upward motion at flight level. However, since the DC-8 sampled this region approximately 8 min before the GH detected significant electric fields, it is not surprising that strong updrafts do not reach flight altitude during the DC-8 sampling period.

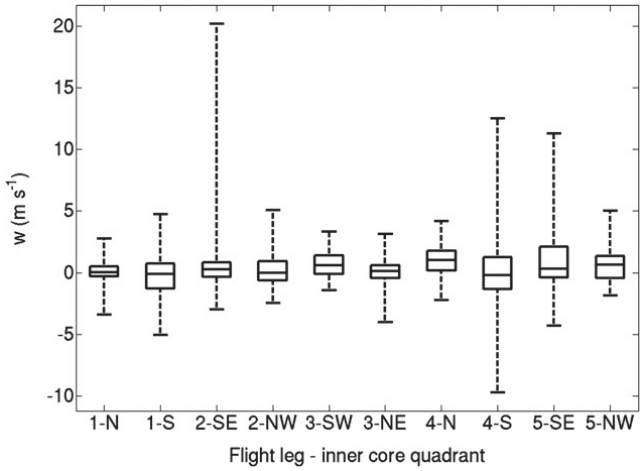

FIG. 4. Box and whisker plots of DC-8 flight-level, inner-core vertical velocities measured by the MMS. The x axis contains the flight leg number and the location relative to Karl's eye. Note that the measurements taken during legs 1–2 were at an average altitude of 10.3 km, while legs 3–5 were sampled at an average altitude of 11.3 km. The interquartile range (25th–75th percentile) of the data is marked by the edges of the solid black boxes, while the solid black line within each box denotes the median.

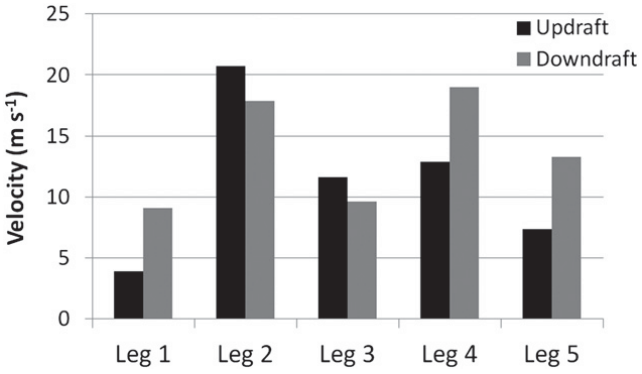

FIG. 5. Maximum updrafts (black) and downdrafts (gray) based on APR-2 Doppler velocity data for each leg, after corrections for terminal velocities were applied. The electrified legs (2–4) all contain peak updrafts that exceed 10 m s^{-1}, while the peak updrafts for nonelectrified legs (1 and 5) are less than 10 m s^{-1}.

Doppler data from the APR-2, after correction for terminal fall speeds, provide vertical motions below DC-8 flight level. Figure 5 displays maximum values of updrafts (black) and downdrafts (gray) for each leg. The maximum updraft along each electrified leg (2–4) exceeds 10 m s^{-1}, with the strongest updraft of 20.7 m s^{-1} occurring during leg 2. On the other hand, maximum updrafts along the nonelectrified legs (1 and 5) are less than 10 m s^{-1}. These results indicate that the strongest vertical motions were located within Karl's electrified inner-core regions.

Peak updrafts in these electrified regions meet or exceed the 10–12 m s^{-1} threshold proposed by Zipser and Lutz (1994) as necessary for rapid storm electrification. The maximum updrafts measured in Karl (>20 m s^{-1}) also are comparable to the strongest updrafts cited in previous studies of TC vertical velocities (Black et al. 1996; Cecil et al. 2010; Guimond et al. 2010; Heymsfield et al. 2010). For example, the average maximum updraft for the 13 TC cases analyzed in Heymsfield et al. (2010) was 18.1 m s^{-1}. However, in the seven Atlantic hurricanes studied by Black et al. (1996), only ~5% of the vertical velocities in the eyewall region exceeded 5 m s^{-1}. Thus, although 10–20 m s^{-1} updrafts do occur in TC convection, their occurrence appears to be rare.

2) CLOUD MICROPHYSICS

The noninductive charging mechanism requires collisions between graupel pellets and lighter ice crystals in the presence of supercooled water (Takahashi 1978; Saunders and Peck 1998; Saunders 2008; Emersic and Saunders 2010). Unfortunately, supercooled water was not directly measured at DC-8 flight level, in part because the flight legs were at temperatures ranging from −32° to −45°C. However, the available cloud microphysics data can be used to characterize the flight-level hydrometeors within Karl's inner core and infer the presence of supercooled water below aircraft altitude.

The CDP and CAS instruments aboard the DC-8 aircraft measured the concentration of small particles (<52.5 μm in diameter) at flight level. Herman and Heymsfield (2003) and A. J. Heymsfield et al. (2006, 2009) found enhanced concentrations of small ice particles (<50 μm) near the strong updrafts of TCs and oceanic convection. Large concentrations of small particles were strongly correlated with updraft strength in Hurricane Humberto (2001; A. J. Heymsfield et al. 2006). Since the small ice particle concentrations observed in these regions were deemed too great to have developed solely by heterogeneous nucleation processes, the authors proposed that nucleation occurred via homogeneous freezing (Herman and Heymsfield 2003; Heymsfield et al. 2009). Figure 6 illustrates this process near the −40°C level of a deep convective storm. The presence of recently frozen, homogeneously nucleated ice particles at flight level implies that supercooled droplets were present below the aircraft in order to be frozen at flight level. This information can help explain the presence/absence of lightning within different regions of Karl.

We examined the relationship between small particle concentrations and vertical velocities in Karl on 16 September. Since particle concentrations were sampled at 5-s intervals, they were matched with corresponding 1-s MMS vertical velocities. CDP/CAS concentration and updraft speed exhibit a moderate positive correlation (r = 0.69 and 0.56, respectively). This relationship

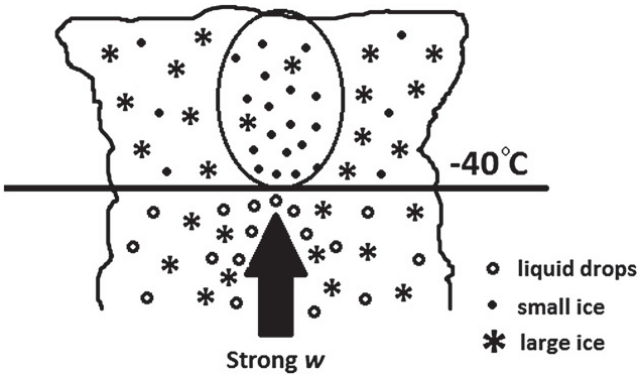

FIG. 6. Conceptual illustration of small, homogeneously nucleated ice particles (circled) being lofted above the −40°C level by a strong thunderstorm updraft. These recently frozen ice particles suggest that supercooled water may exist below the −40°C level.

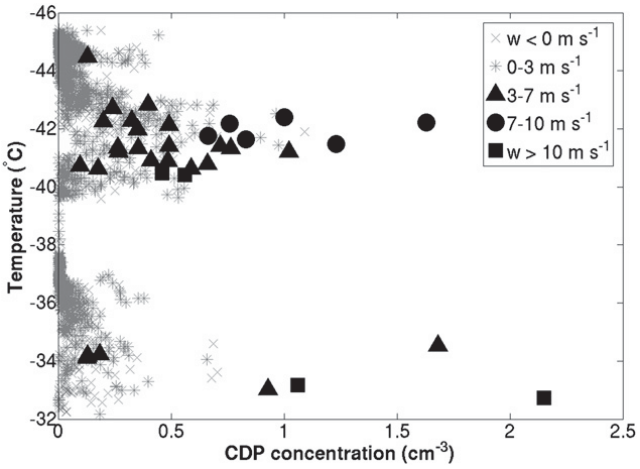

FIG. 7. CDP concentration (cm^{-3}) plotted vs temperature (°C) between 1900 and 2300 UTC. Different symbols represent the corresponding vertical velocity for each measurement. Greater CDP concentrations generally are associated with moderate to strong updrafts.

is further explored in Fig. 7, which shows variations between CDP number concentration, temperature, and vertical velocity. The greater small particle concentrations clearly are associated with moderate to strong updrafts. Although all the hydrometeors at flight level were frozen, these pulses of small ice particles indicate regions where supercooled droplets may exist below aircraft altitude (as illustrated in Fig. 6). As shown later, greater concentrations of small, homogeneously nucleated ice particles often were observed within electrified regions of Karl.

3) RADAR REFLECTIVITY

Previous studies have shown that TC/oceanic convection generally exhibits modest reflectivities that decrease rapidly above the freezing level (Jorgensen et al. 1985; Szoke et al. 1986; Marks and Houze 1987; Zipser and Lutz 1994; Petersen et al. 1996, 1999; Cecil et al. 2002; Rogers et al. 2007). These findings are consistent with weak TC updrafts that rapidly become glaciated above 0°C (Jorgensen et al. 1985; Black and Hallett 1986). Because water has a greater dielectric constant than ice, liquid droplets produce greater reflectivities than ice particles of similar size. Therefore, enhanced reflectivity in the mixed-phase region (0° to −20°C layer) indicates the presence of supercooled water and/or large ice particles above the freezing level. Greater reflectivities in the mixed-phase region also suggest an increased probability of lightning in TCs and oceanic convection (Petersen et al. 1996, 1999; Cecil and Zipser 2002). We used APR-2 data to study the variability of reflectivity profiles along the electrified and nonelectrified legs of Karl.

Figure 8 shows contoured frequency by altitude diagrams (CFADs; cf. Fig. 5 of LeMone and Zipser 1980) of reflectivity in the convective regions of nonelectrified leg 1 (Fig. 8a) and electrified leg 2 (Fig. 8b), as well as 90th-percentile reflectivity profiles (Fig. 8c) for each of the five legs. Since the APR-2 performs cross track scans, we selected the most nadir of each set of scans for this analysis. As could be expected from the vertical velocity differences shown in Figs. 4 and 5, the reflectivity distributions for legs 1 and 2 are quite different. The sharp increase in reflectivity near 5 km (the radar bright band) in Fig. 8a indicates the height of the freezing level and suggests that the convection along leg 1 was transitioning to stratiform precipitation. The reflectivities for leg 2 (Fig. 8b) are shifted to larger values from the near surface to 9 km, and there is evidence of enhanced reflectivities above the freezing level (~5 km). This suggests that supercooled water and/or large ice particles are being lofted well above the freezing level, which would be expected in a convective region actively producing lightning. The 90th percentile reflectivity profiles for all legs (Fig. 8c) show that the electrified legs (2–4) have greater inner-core reflectivities than the nonelectrified legs (1 and 5) both above and below 0°C.

b. Case study: Electrified leg 2 (1940–2000 UTC)

Leg 2 was an electrified southeast to northwest flight segment through Karl from 1940 to 2000 UTC. The DC-8 and GH were well coordinated during this pass, and the global lightning networks detected numerous flashes within Karl's southeast eyewall during the sampling period (Fig. 9). The excellent coordination on this leg enabled us to thoroughly analyze the electrified southeast eyewall using data from both aircraft.

We used HAMSR brightness temperatures to assess Karl's convective structure during leg 2. Since the depression of microwave brightness temperature T_B due to ice scattering is greater at high frequencies than low

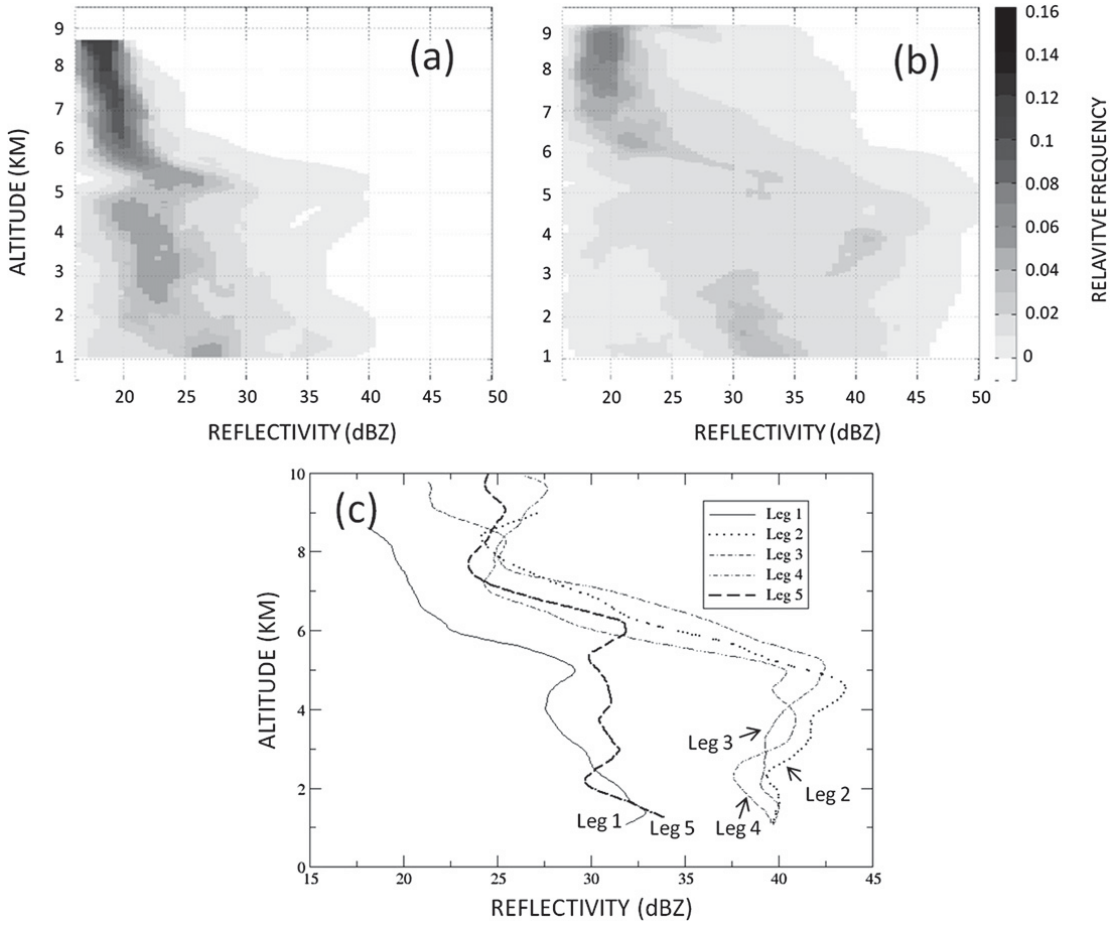

FIG. 8. CFADs for the APR-2 reflectivity of convective regions along (a) leg 1 and (b) leg 2, as well as (c) 90th percentile reflectivity profiles for each of the five legs. On leg 1, the reflectivity generally decreases with height, and a brightband signature is clearly visible around 5 km (indicative of more stratiform precipitation). On leg 2, higher reflectivities occur more frequently throughout the troposphere, including the mixed-phase region above 5 km. The electrified legs (2–4) have greater reflectivities than the nonelectrified legs (1 and 5) throughout the troposphere.

frequencies, large differences between high- and low-frequency T_B indicate where deep convection is occurring (Brown et al. 2007). Figure 10 depicts large 50.30-/113.25-GHz T_B differences in the southeast eyewall, confirming that this region contains deep convection. We will focus on this portion of leg 2 in the following case study.

Figure 11 shows electric field measurements recorded by LIP along leg 2. This image is similar to Fig. 6 of Mach et al. (2009), Fig. 5 of Cecil et al. (2010), and Fig. 3 of Mach et al. (2010), which all described electrified overflights during previous field campaigns. Most electrified continental and maritime convection (i.e., storms with a normal tripole vertical charge structure) exhibits positive electric fields above the storm (Stolzenburg et al. 1998; MacGorman and Rust 1998; Williams 2009; Mach et al. 2009). The blue lines in Fig. 11a depict the *x*–*y* components of the field, with the vectors extending outward from the flight track away from the positive charge aloft. Vector length represents the strength of the electric field at points along the flight path. Figures 11b and 11c are longitude–altitude and latitude–altitude plots, respectively, that depict the vertical components of the electric field in the east–west and north–south directions. So, Fig. 11 provides a three-dimensional view of the electrical structure measured by LIP. The orientation of the electric field vectors in Fig. 11a reveals that the charged convection around 1948 UTC is located just northeast of the GH flight path, while Figs. 11b and 11c indicate that the positive charge center is located below the aircraft.

Although WWLLN detected numerous flashes near the GH aircraft (Fig. 11a, gold stars), LIP electric field analysis only revealed two flashes along this leg (Fig. 9). However, LIP's relatively small flash count may be attributed to the ''shower effect,'' in which a large storm near the sensors masks field changes from lightning farther from the aircraft. The WWLLN lightning flashes

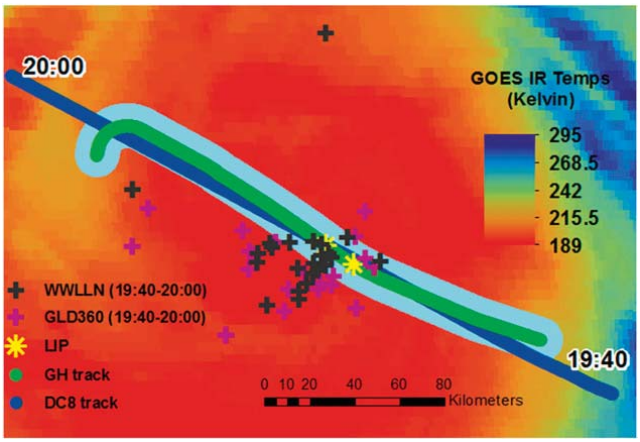

FIG. 9. GRIP aircraft tracks and WWLLN/GLD360 lightning flashes between 1940 and 2000 UTC overlaid on 1945 UTC GOES IR imagery of Karl. The gold stars designate the location of the GH when LIP detected lightning flashes. A 10-km buffer (light blue) is placed along the GH flight track to highlight WWLLN and GLD360 flashes near the aircraft.

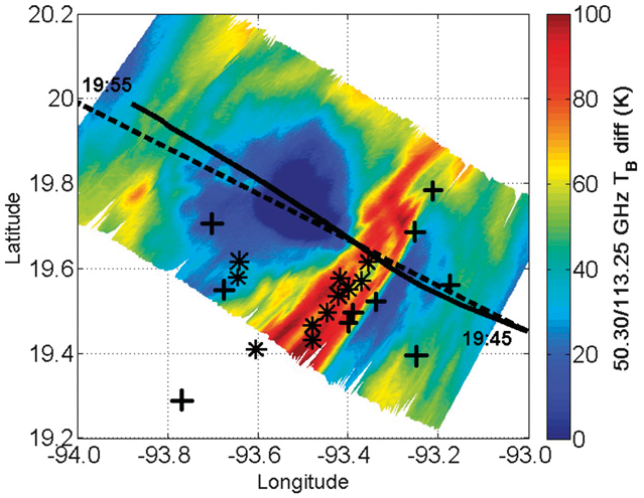

FIG. 10. The T_B differences between the 50.30- and 113.25-GHz channels of HAMSR from 1945 to 1955 UTC. Large T_B differences (red) in the southeast eyewall indicate regions where greater ice scattering, and thus deep convection, are occurring. WWLLN [asterisk (*)] and GLD360 [plus (+)] flashes from 1945 to 1955 UTC, as well as GH (solid) and DC-8 (dashed) flight tracks, are overlaid for reference.

(gold stars) overlaid on Fig. 11a suggest that lightning was concentrated on the left side of the GH flight path, which seems to conflict with the storm location indicated by the LIP electric fields. There are several possible explanations for this location difference: 1) the global networks may not be locating the lightning flashes precisely, 2) there may be flashes on the east side of the flight track that the global networks do not detect, or 3) the location of the CG flashes may be displaced from the positive thunderstorm charge aloft detected by the LIP. Regardless, it is clear that the GRIP aircraft penetrated an electrically active region during this leg.

Vertical reflectivity data from APR-2 and HIWRAP help characterize the structure of Karl's inner-core convection. Although both radars measure Ku-band (~13 GHz) reflectivity, they employ different scan strategies. APR-2 has a downward-pointing antenna that scans across the aircraft track (Sadowy et al. 2003). Near-nadir scans can be identified based on the orientation of the aircraft. Conversely, HIWRAP has a conical scan configuration, with the inner/outer beams tilted 30° and 40°, respectively, from the vertical (G. M. Heymsfield et al. 2006). The Ku-band HIWRAP reflectivity presented here is the 30° incidence angle data mapped to the vertical section.

Reflectivities from APR-2 (Fig. 12a) and HIWRAP (Fig. 13) show a deep convective cell within Karl's southeast eyewall. This was the focus of the electrical activity observed along leg 2. APR-2 on the DC-8 aircraft shows a cell with enhanced reflectivity aloft and a 35-dBZ region extending several kilometers above the freezing level. HIWRAP on the GH aircraft reveals that the eyewall convection extends well above 12 km. Figure 12b shows the dual-wavelength ratio (DWR), which is the difference between the Ku-band (13.4 GHz) and Ka-band (35.6 GHz) observed reflectivities. DWR typically is near 0 dB for small ice particles (i.e., particles are small enough to be in the Rayleigh regime at both wavelengths). DWR becomes increasingly positive for larger particles as non-Rayleigh effects reduce the Ka-band reflectivity (see the regions above 0°C), or when the presence of liquid water introduces differential attenuation (particularly noticeable in the rain layer). Enhanced reflectivity aloft is a good indicator that graupel and supercooled water are being carried far above the freezing level by strong updrafts (e.g., Zipser and Lutz 1994), and the collocated presence of large DWR strengthens this assessment.

APR-2 total Doppler velocities (Fig. 12c) show significant updrafts above the freezing level, with compensating downdrafts aloft and strong downdrafts near the surface. Note that negative values in Fig. 12c represent upward vertical motion, and that no terminal velocity correction has been applied. Therefore, upward (downward) vertical motions appear weaker (stronger) than true air velocities. Recall that the maximum DC-8 flight-level updraft (Fig. 4) and the maximum updraft derived from APR-2 velocities (Fig. 5) both exceed 20 m s^{-1} in this convective region, the strongest vertical motions sampled on this day. Figure 12d contains an experimental microphysics classification product produced by the APR-2 suite of retrieval algorithms. The

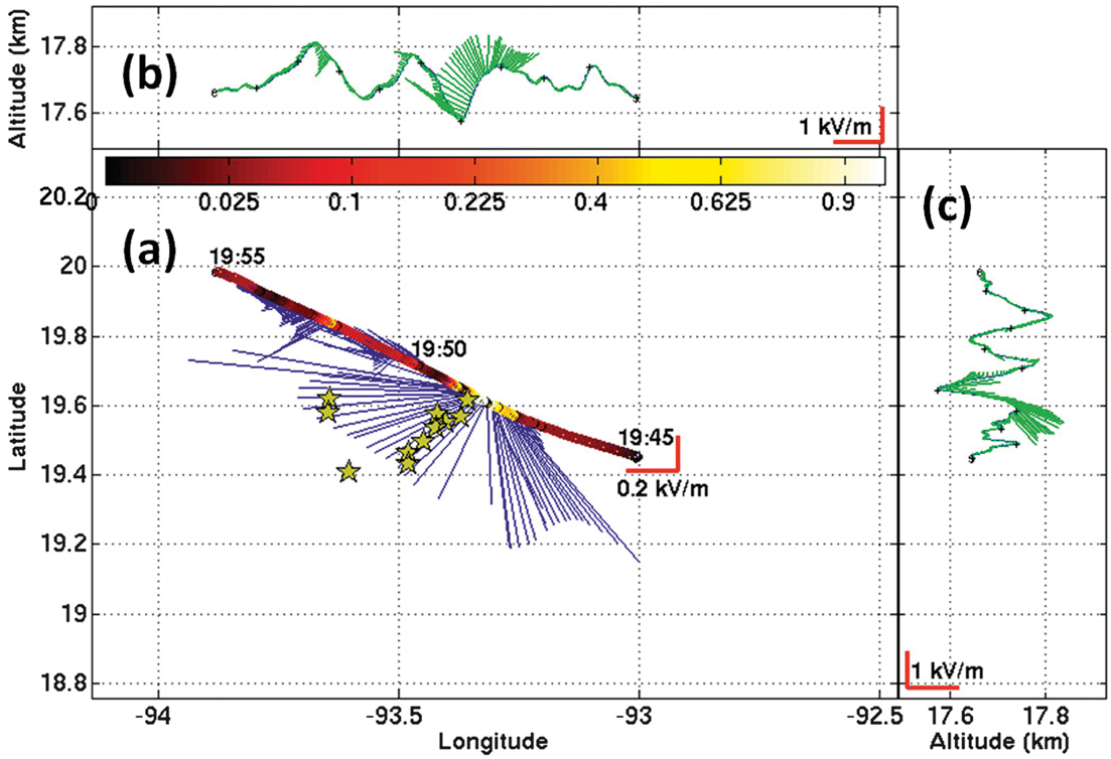

FIG. 11. LIP electric field measurements between 1945 and 1955 UTC. (a) Two-dimensional electric field vectors (blue) along the GH flight track. The vectors point away from the positive charge center of the storm that is located northeast of the GH around 1948 UTC. Colors along the flight path indicate the strength of the vertical electric field (color bar). Yellow stars denote WWLLN lightning flashes (1945–1955 UTC). (b) Vertical and east/west components of the electric field (green vectors). (c) Vertical and north/south components of the electric field (green vectors). For reference, the peak electric field measured on this flight leg was approximately 2.15 kV m^{-1}.

product uses APR-2 reflectivity, Doppler velocity, and cross-polarization data to classify scattering particles as rain, snow, graupel, or ice. Tanelli et al. (2004) provide details on an earlier version of this precipitation classification algorithm. Figure 12d shows a region of dry graupel (indicated by the orange color) collocated with the reflectivity core that extends several kilometers above the freezing level, which is located near 5 km. This configuration is expected in electrically active convection. We will analyze the cloud microphysics of this region in greater detail later.

An analysis of lightning flashes in the eyewall reveals a cluster of WWLLN-derived inner-core flashes that rotates in a counterclockwise direction around Karl's center (Fig. 14). Intense convective bursts, or convective events, produced similar patterns of IC lightning in the eyewalls of Hurricanes Katrina and Rita (2005; Fierro et al. 2011). Geostationary Operational Environmental Satellite (GOES) IR satellite imagery (Fig. 15) shows a small region of intense convection with cloud top $T_B <$ −80°C rotating counterclockwise around Karl's eyewall at a speed of approximately 20 m s^{-1}. The shaded WWLLN lightning activity in Fig. 14 corresponds with the relative location and movement of the deep convection highlighted in Fig. 15. The satellite and lightning data indicate that this convective burst persists for approximately 30 min.

Recent observational (Guimond et al. 2010) and modeling (Fierro et al. 2007; Fierro and Reisner 2011) studies have shown evidence of deep convective bursts preceding the rapid intensification of some TCs. The convective bursts in Guimond et al. (2010) contained maximum updrafts of 20 m s^{-1} at altitudes of 12–14 km, with strong downdrafts flanking the updrafts. The simulated convective events of Fierro and Reisner (2011) contained updrafts exceeding 10 m s^{-1} and propagated at speeds approximately 10 m s^{-1} less than the azimuthal flow in the eyewall. The convective events tracked in Fierro et al. (2011) had lifetimes ranging from 12 to 40 min. These characteristics are very similar to those of Karl's deep convection during leg 2. Therefore, the data suggest that the GRIP aircraft did penetrate a deep convective burst embedded within Karl's eyewall.

We next use CDP (2.5–51 μm) and CAS (0.58–52.5 μm) particle concentration data in conjunction with 2D images from PIP (hydrometeors up to 6.4 mm) to analyze

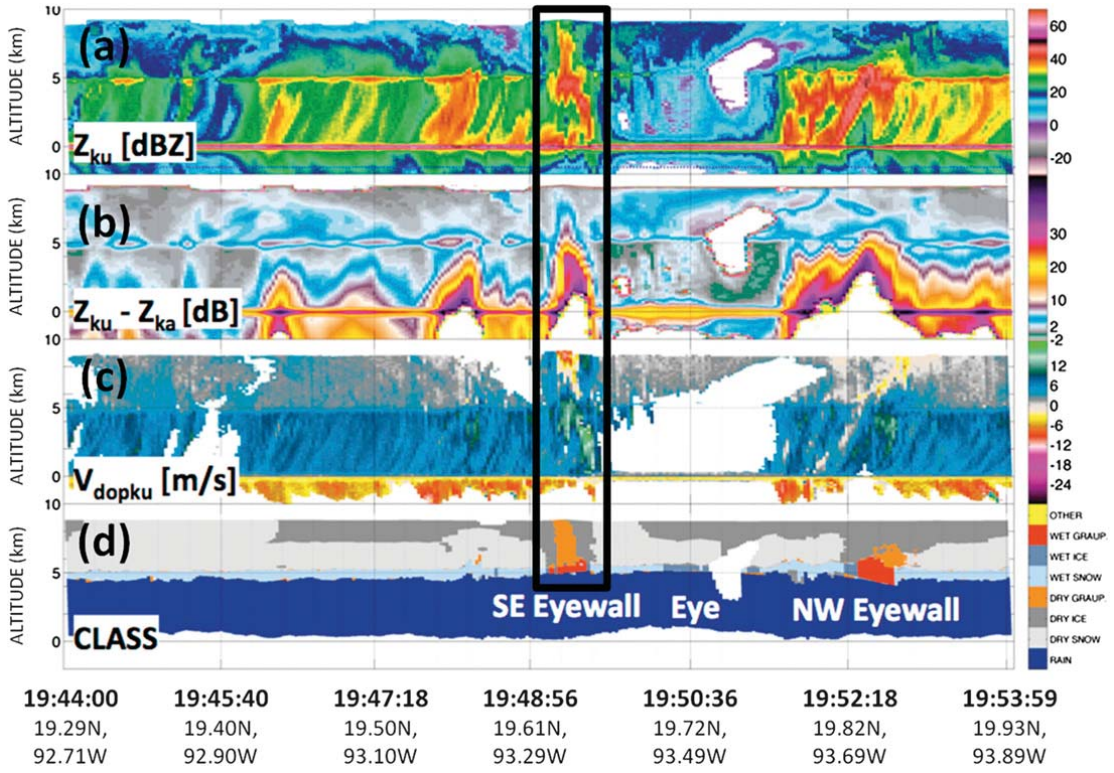

FIG. 12. APR-2 data from a southeast to northwest pass through Karl between 1944:00 and 1953:59 UTC. (a) Ku-band reflectivity. (b) Dual wavelength ratio (difference between Ku-band and Ka-band observed reflectivities). (c) Total Doppler velocity, with negative values representing upward vertical motion. (d) APR-2 experimental microphysics classification product. The black box highlights the electrified convective region of interest.

the microphysics of this electrified region. Figure 16 is a time series of CDP and CAS concentrations as well as MMS vertical velocities. The sharp increase in CDP and CAS concentrations just after 1949 UTC corresponds to the time of the 20 m s^{-1} updraft measured during this leg. In fact, the greatest small particle concentrations and vertical velocity sampled during the entire flight occurred here on leg 2. The collocation of very small ice particles and strong updrafts are consistent with the findings of Herman and Heymsfield (2003) and A. J. Heymsfield et al. (2006).

Particle shattering issues on the CAS explain the two orders of magnitude difference between the CAS and CDP ice concentrations in Fig. 16. Since the CAS (CDP) probe is known to overestimate (underestimate) ice concentration, the true amount of small ice probably is between the CAS and CDP values. Even taking the CDP value as a lower bound estimate, the concentration of these small particles is likely too great to have occurred solely by heterogeneous nucleation processes (Herman and Heymsfield 2003; A. J. Heymsfield et al. 2006), thus implying that homogeneous freezing was another mechanism for ice production in this region of the eyewall. Since homogeneous nucleation occurs near temperatures of −40°C, the small ice particles measured at DC-8 flight level likely were recently frozen. This further supports our previously stated inference that supercooled water was located somewhere below the DC-8 as it penetrated the core of the electrified convection.

Figure 17 contains images of particles sampled by PIP at various locations in the southeast quadrant of Karl.

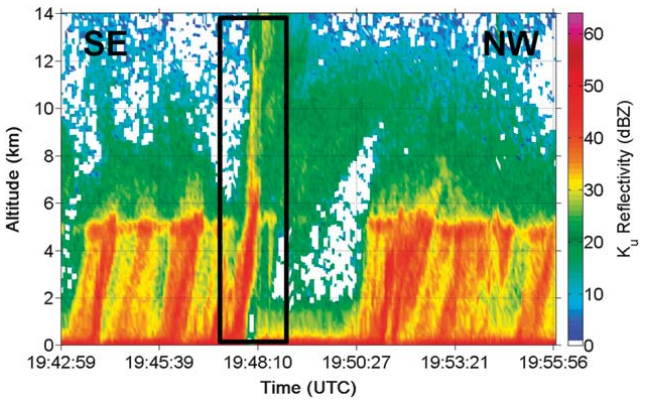

FIG. 13. Ku-band HIWRAP reflectivity data between 1942:59 and 1955:56 UTC. The black box denotes the electrified convective region of interest. Recall that the tilted appearance of the reflectivity is due to the scan geometry of HIWRAP.

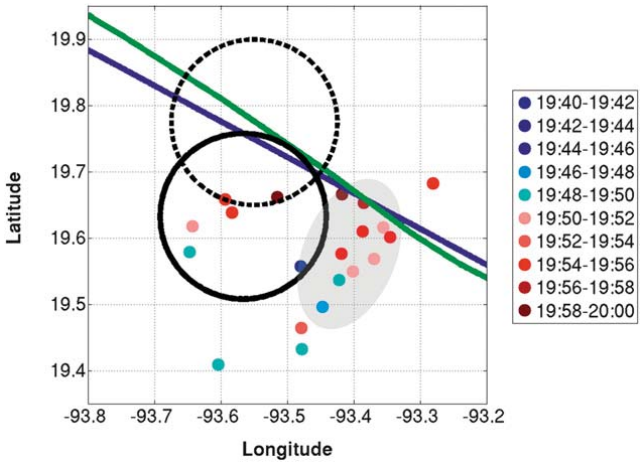

FIG. 14. WWLLN-derived inner-core flashes between 1940 and 2000 UTC color coded by time of occurrence, similar to Fig. 4 in Fierro et al. (2011). Tracks of the DC-8 (blue) and GH (green) are overlaid. The solid black circle represents the estimated location and size of Karl's eye based on National Hurricane Center (NHC) data. Because the locations of several flashes are not consistent with the NHC location, the dashed circle shows the location of Karl's eye inferred from satellite, HAMSR, and lightning data. The location differences could be attributed to WWLLN position errors (see earlier section) and/or NHC location errors. The shaded region highlights a cluster of flashes (a deep convective burst) rotating counterclockwise around Karl's eye in the southeast eyewall.

Figures 17a and 17d reveal that small ice particles and aggregates are present on either side of the deep convection; however, there is no indication of graupel. In contrast, Figs. 17b and 17c show greater concentrations of small ice particles collocated with 1–2-mm graupel particles (circled in red). The location of the graupel particles within the convective region is consistent with the microphysics classification product shown in Fig. 12d. The enhanced concentrations of small homogeneously nucleated ice particles at flight level further support the inference of supercooled water below the aircraft in this electrified region (Herman and Heymsfield 2003). A convective environment with small ice, large graupel, and supercooled water is certainly conducive to charge separation and TC electrification (e.g., Black and Hallett 1999).

APR-2 radar data further support this microphysical analysis. Representative vertical profiles of Ku- and Ka-band measured reflectivities (Z_a; Fig. 18) were extracted from the center of the convective updraft region around 1949 UTC. We can identify four distinct layers in these profiles. Above 8.7 km (layer 1), Z_a at both wavelengths indicates particles in the Rayleigh regime (i.e., mean mass weighted particle sizes smaller than 1 mm). Larger particles are present at this altitude in nearby profiles, though not at this particular location. As one may expect in the presence of turbulent regimes, the large and small particles were distributed nonhomogenously in the upper portion of this convective core. Between 8.7 and 7.2 km (layer 2), both Z_a increase by several decibels and the DWR increases to ~6 dB, indicating that the mean ice particle size has increased to approximately 5 mm in this layer.

From 7.2 to 5.5 km (layer 3), the DWR keeps increasing, but both profiles exhibit a marked difference in slope compared to those in the 8.7–7.2-km layer. This indicates the onset of attenuation in the Ka-band channel. This behavior can be explained by the presence of dry graupel particles becoming increasingly large toward the bottom of the layer (reaching average sizes near 1 cm). This profile could also suggest the presence of cloud liquid water in amounts up to 0.5 g m^{-3} and graupel particles with mean sizes between 5 mm and 1 cm. Either way, cloud liquid water must have been present well above 0°C to produce the large graupel particles noted here. Below 5.5 km (layer 4), attenuation increases rapidly, first in the Ka band then the Ku band. This is consistent with the transition to liquid-phase hydrometeors. The absence of the typical radar brightband signature confirms that the frozen hydrometeors above this layer were graupel or hail and not low-density aggregates.

4. Summary and conclusions

This study has examined the microphysical and kinematic properties that contributed to the presence of lightning in Hurricane Karl on 16 September 2010. Numerous datasets (Table 1) collected by the NASA DC-8 and Global Hawk aircraft during the 2010 NASA GRIP experiment were used to analyze Karl's vertical motions, cloud microphysics, and radar-derived storm structure. We then examined how these properties varied along five flight legs through electrified and nonelectrified inner-core regions of the storm (Table 2), as determined by LIP, GLD360, and WWLLN lightning data.

Flight-level vertical velocities from the MMS (Fig. 4) and Doppler-derived vertical velocities from the APR-2 (Fig. 5) revealed that Karl's electrified inner-core regions typically contained peak updrafts exceeding 10 m s^{-1}, with some as strong as 20 m s^{-1}. These findings are consistent with previous studies (Zipser and Lutz 1994; Black and Hallett 1999; Fierro et al. 2007) that related strong vertical motions to enhanced TC lightning activity. Conversely, the nonelectrified regions of Karl's inner core generally were associated with weaker updrafts that peaked around 5–7 m s^{-1}. Concentrations of small ice particles ($<52.5\ \mu$m in diameter) exhibited a moderate positive correlation with updraft speed, and the greatest concentrations often were associated with moderate to

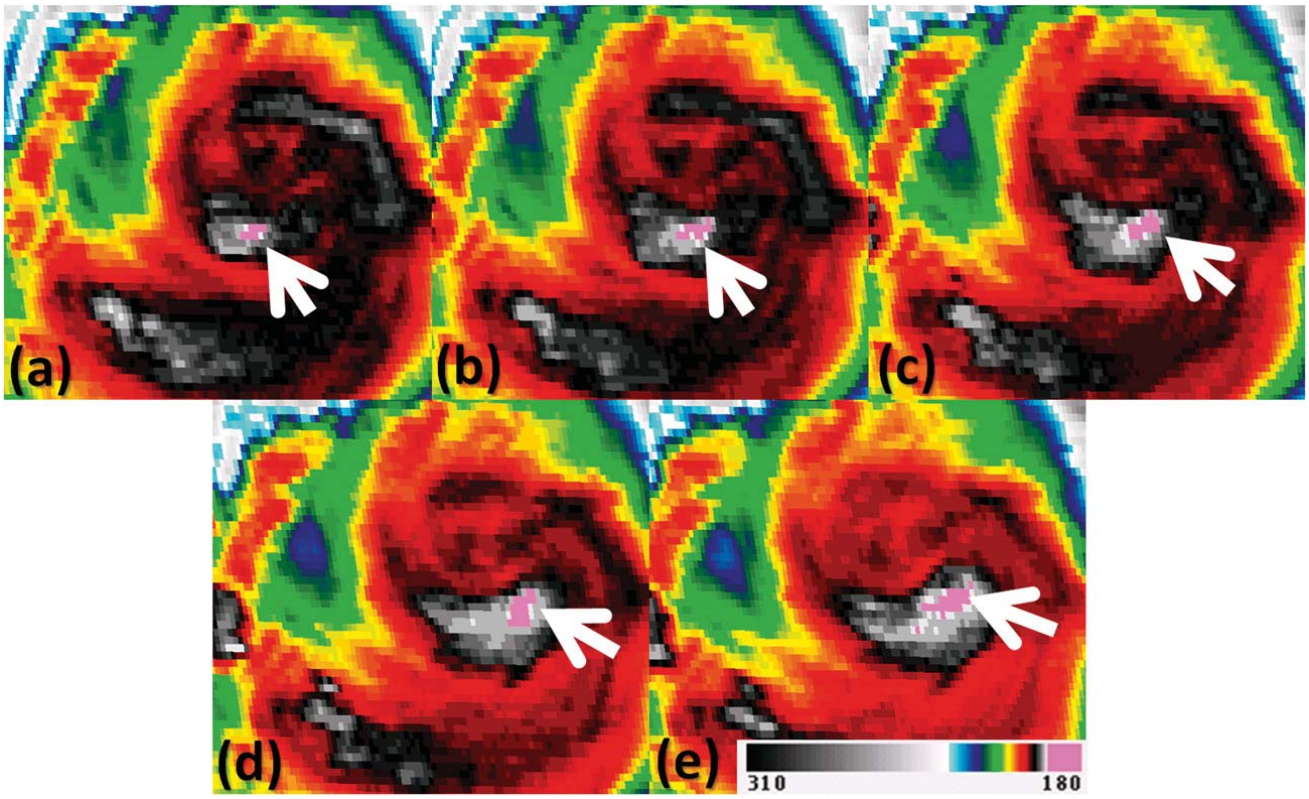

FIG. 15. GOES 10.7-μm IR satellite images of Hurricane Karl on 16 Sep: (a) 1932, (b) 1940, (c) 1945, (d) 1955, and (e) 2003 UTC. The pink color corresponds to IR cloud-top brightness temperatures colder than -80°C. The white arrows in each panel follow the deep convective burst moving counterclockwise around the eyewall at approximately 20 m s^{-1}.

strong updrafts (Fig. 7). As in previous TC microphysical studies (Herman and Heymsfield 2003; A. J. Heymsfield et al. 2006), the greatest concentrations of small ice were deemed too large to have occurred solely by heterogeneous nucleation. It is likely that some of these ice particles at flight level (10.3–11.3 km) were recently frozen (Herman and Heymsfield 2003), suggesting that supercooled water existed below the aircraft. The presence of supercooled water above the freezing level is critical for charge separation and storm electrification (e.g., Takahashi 1978; Black and Hallett 1999; Saunders 2008).

Data from the APR-2 (Fig. 8) revealed that the electrified legs contained reflectivities several decibels greater than the nonelectrified legs throughout most of the troposphere. The enhanced reflectivities in the mixed-phase region of these electrified legs indicated that supercooled water and/or large ice particles were being carried aloft by the strong updrafts. Enhanced reflectivity above the freezing level is a good indicator of deep convection whose strong updrafts produce an environment conducive to electrification (Zipser and Lutz 1994; Petersen et al. 1996, 1999; Cecil and Zipser 2002; Cecil et al. 2010). These radar signatures were consistent with the in situ microphysical data and the inference of supercooled water in the electrified inner-core regions.

The case study of leg 2 analyzed properties of the electrified inner-core region in detail. During leg 2

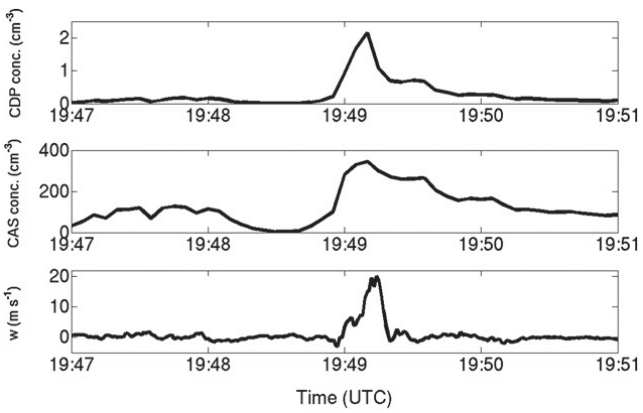

FIG. 16. Time series of (top) CDP concentration (cm^{-3}), (middle) CAS concentration (cm^{-3}), and (bottom) vertical velocity (m s^{-1}) from 1947 to 1951 UTC. The sudden increase in small ice particle concentrations matches the time of the 20 m s^{-1} updraft. The two orders of magnitude difference between the CAS and CDP ice concentrations is due to known particle shattering issues on the CAS probe.

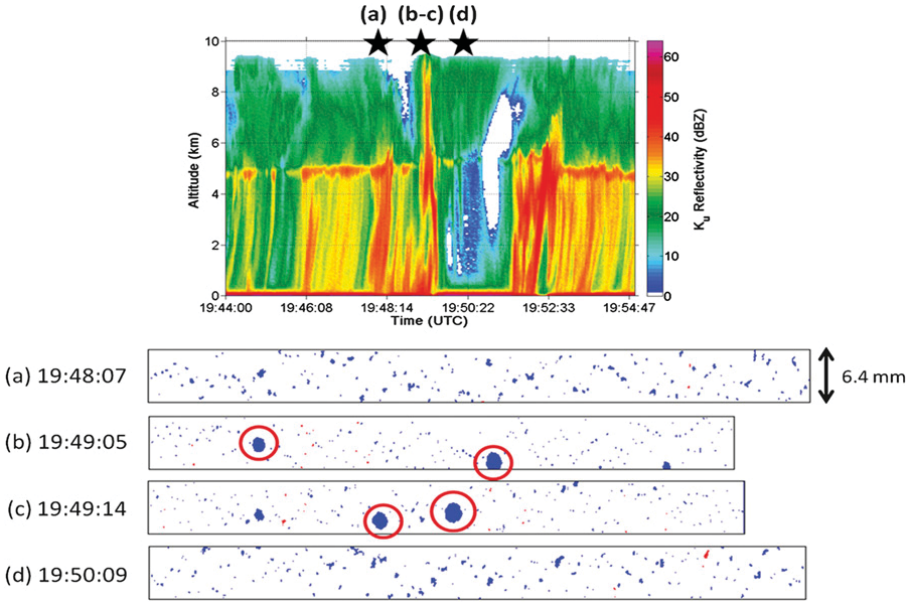

FIG. 17. PIP particle images from the southeast eyewall of Karl: (a) 1948:07, (b) 1949:05, (c) 1949:14, and (d) 1950:09 UTC. The black stars on top of the radar scan indicate the approximate location where each particle image was taken. Red circles identify graupel particles present in the convective region.

(Fig. 9), the GRIP aircraft sampled a deep convective burst that produced lightning in Karl's southeast eyewall (Figs. 14, 15). Despite structural differences between the convection sampled on leg 2 and the other electrified legs, we identified several common characteristics among all of Karl's electrified regions. Our results show that the electrified inner-core regions generally were associated with 1) strong updrafts of 10–20 m s^{-1} (Figs. 4, 5, 12c); 2) deep mixed-phase layers indicated by reflectivities >30 dBZ extending several kilometers above the freezing level (Figs. 12a and 13); and 3) microphysical environments consisting of graupel, very small ice particles, and the inferred presence of supercooled water (Figs. 12b, 12d, 16, 17, 18). These characteristics describe an environment favorable for noninductive charging (Takahashi 1978; Saunders and Peck 1998; Saunders 2008; Emersic and Saunders 2010) and, therefore, TC electrification (Black and Hallett 1999). We conclude that the electrified regions in Karl's inner core were attributable to a microphysical environment that was conducive to electrification because of occasional, strong convective updrafts in Karl's eyewall.

This study capitalized on the unique opportunity provided by GRIP to synthesize multiple datasets from two aircraft and thereby analyze the microphysical and kinematic properties of an electrified TC. The ability to monitor TC lightning globally, continuously, and remotely makes lightning data a potentially valuable resource that demands further investigation on future hurricane field campaigns. With the upcoming launch of the Geostationary Lightning Mapper (GLM; Goodman et al. 2013) aboard the GOES R-series (GOES-R), unprecedented total lightning data will become available to support future TC electrification studies.

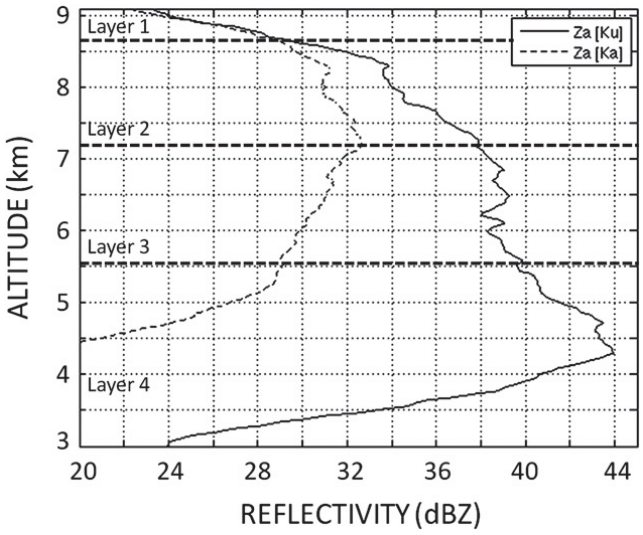

FIG. 18. Vertical profiles of Ku-band (solid) and Ka-band (dashed) measured reflectivities Z_a from the electrified convective region sampled on leg 2 around 1949 UTC. The behavior of the Ku- and Ka-band reflectivities in layer 3 (7.2–5.5 km) supports the presence of large graupel and cloud liquid water above 0°C near the updraft region.

Acknowledgments. We wish to thank the many people who made the GRIP project and this resulting research possible. The research at Florida State University was supported by NASA Grant NNX09AC43G and an AMS/Northrop Grumman Graduate Fellowship to the lead author. A portion of this research (Durden, Lambrigtsen, and Tanelli) was carried out at the Jet Propulsion Laboratory, California Institute of Technology, under a contract with the National Aeronautics and Space Administration. The authors wish to thank the World Wide Lightning Location Network (http://wwlln.net), a collaboration among over 50 universities and institutions, for providing lightning location data used in this paper.

REFERENCES

Abarca, S. F., K. L. Corbosiero, and T. J. Galarneau Jr., 2010: An evaluation of the Worldwide Lightning Location Network (WWLLN) using the National Lightning Detection Network (NLDN) as ground truth. *J. Geophys. Res.,* **115,** D18206, doi:10.1029/2009JD013411.

——, ——, and D. Vollaro, 2011: The World Wide Lightning Location Network and convective activity in tropical cyclones. *Mon. Wea. Rev.,* **139,** 175–191.

Austin, M. D., and H. E. Fuelberg, 2010: Assessment of synoptic and microphysical parameters related to lightning in tropical cyclones and storm intensification. Preprints, *29th Conf. on Hurricanes and Tropical Met.,* Tucson, AZ, Amer. Meteor. Soc., 16D.4. [Available online at https://ams.confex.com/ams/29Hurricanes/webprogram/Paper168972.html.]

Baumgardner, D., H. Jonsson, W. Dawson, D. O'Connor, and R. Newton, 2001: The cloud, aerosol and precipitation spectrometer: A new instrument for cloud investigations. *Atmos. Res.,* **59–60,** 251–264.

Black, M. L., R. W. Burpee, and F. D. Marks Jr., 1996: Vertical motion characteristics of tropical cyclones determined with airborne Doppler radial velocities. *J. Atmos. Sci.,* **53,** 1887–1909.

Black, R. A., and J. Hallett, 1986: Observations of the distribution of ice in hurricanes. *J. Atmos. Sci.,* **43,** 802–822.

——, and ——, 1999: Electrification of the hurricane. *J. Atmos. Sci.,* **56,** 2004–2028.

——, H. B. Bluestein, and M. L. Black, 1994: Unusually strong vertical motions in a Caribbean hurricane. *Mon. Wea. Rev.,* **122,** 2722–2739.

——, G. M. Heymsfield, and J. Hallett, 2003: Extra large particle images at 12 km in a hurricane eyewall: Evidence of high-altitude supercooled water? *Geophys. Res. Lett.,* **30,** 2124, doi:10.1029/2003GL017864.

Blakeslee, R. J., D. M. Mach, M. G. Bateman, and J. C. Bailey, 2014: Seasonal variations in the lightning diurnal cycle and implications for the global electric circuit. *Atmos. Res.,* **135–136,** 228–243, doi:10.1016/j.atmosres.2012.09.023.

Braun, S., and Coauthors, 2013: NASA's Genesis and Rapid Intensification Processes (GRIP) Field Experiment. *Bull. Amer. Meteor. Soc.,* **94,** 345–363.

Brown, S., B. Lambrigtsen, A. Tanner, J. Oswald, D. Dawson, and R. Denning, 2007: Observations of tropical cyclones with a 60, 118 and 183 GHz microwave sounder. *IEEE Int. Geoscience and Remote Sensing Symp. 2007,* Barcelona, Spain, IEEE, 3317 – 3320, doi:10.1109/IGARSS.2007.4423554.

——, ——, R. F. Denning, T. Gaier, P. Kangaslahti, B. H. Lim, J. M. Tanabe, and A. B. Tanner, 2011: The High-Altitude MMIC Sounding Radiometer for the Global Hawk unmanned aerial vehicle: Instrument description and performance. *IEEE Trans. Geosci. Remote Sens.,* **49,** 3291–3301.

Cecil, D. J., and E. J. Zipser, 2002: Reflectivity, ice scattering, and lightning characteristics of hurricane eyewalls and rainbands. Part II: Intercomparison of observations. *Mon. Wea. Rev.,* **130,** 785–801.

——, ——, and S. W. Nesbitt, 2002: Reflectivity, ice scattering, and lightning characteristics of hurricane eyewalls and rainbands. Part I: Quantitative description. *Mon. Wea. Rev.,* **130,** 769–784.

——, K. R. Quinlan, and D. M. Mach, 2010: Intense convection observed by NASA ER-2 in Hurricane Emily (2005). *Mon. Wea. Rev.,* **138,** 765–780.

Chan, K. R., J. Dean-Day, S. W. Bowen, and T. P. Bui, 1998: Turbulence measurements by the DC-8 meteorological measurement system. *Geophys. Res. Lett.,* **25,** 1355–1358.

DeMaria, M., J. Knaff, M. J. Brennan, J. L. Beven II, R. T. DeMaria, A. B. Schumacher, J. Kaplan, and N. W. S. Demetriades, 2011: Tropical cyclone rapid intensity change forecasting using lightning data during the 2010 GOES-R Proving Ground at the National Hurricane Center. Preprints, *Fifth Conf. on the Meteorological Applications of Lightning Data,* Seattle, WA, Amer. Meteor. Soc., 3.4. [Available online at https://ams.confex.com/ams/91Annual/webprogram/Paper185181.html.]

Demetriades, N. W. S., M. J. Murphy, and J. A. Cramer, 2010a: Validation of Vaisala's Global Lightning Dataset (GLD360) over the continental United States. Preprints, *29th Conf. on Hurricanes and Tropical Meteorology,* Tucson, AZ, Amer. Meteor. Soc., 16D.2. [Available online at https://ams.confex.com/ams/pdfpapers/168042.pdf.]

——, R. L. Holle, S. Businger, and R. D. Knabb, 2010b: Eyewall lightning outbreaks and tropical cyclone intensity change. Preprints, *29th Conf. on Hurricanes and Tropical Meteorology,* Tucson, AZ, Amer. Meteor. Soc., 16D.3. [Available online at https://ams.confex.com/ams/pdfpapers/168543.pdf.]

Emersic, C., and C. P. R. Saunders, 2010: Further laboratory investigations into the relative diffusional growth rate theory of thunderstorm electrification. *Atmos. Res.,* **98,** 327–340.

Fierro, A. O., and J. M. Reisner, 2011: High-resolution simulation of the electrification and lightning of Hurricane Rita during the period of rapid intensification. *J. Atmos. Sci.,* **68,** 477–494.

——, L. M. Leslie, E. R. Mansell, J. M. Straka, D. R. MacGorman, and C. Ziegler, 2007: A high-resolution simulation of microphysics and electrification in an idealized hurricane-like vortex. *Meteor. Atmos. Phys.,* **98,** 13–33, doi:10.1007/s00703-006-0237-0.

——, X. Shao, T. Hamlin, J. M. Reisner, and J. Harlin, 2011: Evolution of eyewall convective events as indicated by intracloud and cloud-to-ground lightning activity during the rapid intensification of Hurricanes Rita and Katrina. *Mon. Wea. Rev.,* **139,** 1492–1504.

Goodman, S. J., and Coauthors, 2013: The GOES-R Geostationary Lightning Mapper (GLM). *Atmos. Res.,* **125–126,** 34–49.

Guimond, S. R., G. M. Heymsfield, and F. J. Turk, 2010: Multiscale observations of Hurricane Dennis (2005): The effects of hot towers on rapid intensification. *J. Atmos. Sci.,* **67,** 633–654.

Herman, R. L., and A. J. Heymsfield, 2003: Aircraft icing at low temperatures in Tropical Storm Chantal (2001). *Geophys. Res. Lett.,* **30,** 1955, doi:10.1029/2003GL017746.

Heymsfield, A. J., A. Bansemer, S. L. Durden, R. L. Herman, and T. P. Bui, 2006: Ice microphysics observations in Hurricane Humberto: Comparison with non-hurricane-generated ice cloud layers. *J. Atmos. Sci.,* **63,** 288–308.

——, ——, G. M. Heymsfield, and A. O. Fierro, 2009: Microphysics of maritime tropical convective updrafts at temperatures from −20° to −60°C. *J. Atmos. Sci.,* **66,** 3530–3562.

Heymsfield, G. M., J. R. Carswell, L. Li, D. Schaubert, and J. Creticos, 2006: Development of the High-Altitude Imaging Wind and Rain Airborne Profiler (HIWRAP). *Eos, Trans. Amer. Geophys. Union,* **87** (Fall Meet. Suppl.), Abstract IN21A-1202.

——, L. Tian, A. J. Heymsfield, L. Li, and S. Guimond, 2010: Characteristics of deep tropical and subtropical convection from nadir-viewing high-altitude airborne Doppler radar. *J. Atmos. Sci.,* **67,** 285–308.

Houze, R. A., Jr., F. D. Marks Jr., and R. A. Black, 1992: Dual-aircraft investigation of the inner core of Hurricane Norbert. Part II: Mesoscale distribution of ice particles. *J. Atmos. Sci.,* **49,** 943–962.

Hutchins, M. L., R. H. Holzworth, J. B. Brundell, and C. J. Rodger, 2012: Relative detection efficiency of the World Wide Lightning Location Network. *Radio Sci.,* **47,** RS6005, doi:10.1029/2012RS005049.

Jorgensen, D. P., and M. A. LeMone, 1989: Vertical velocity characteristics of oceanic convection. *J. Atmos. Sci.,* **46,** 621–640.

——, E. J. Zipser, and M. A. LeMone, 1985: Vertical motions in intense hurricanes. *J. Atmos. Sci.,* **42,** 839–856.

LeMone, M. A., and E. J. Zipser, 1980: Cumulonimbus vertical velocity events in GATE. Part I: Diameter, intensity, and mass flux. *J. Atmos. Sci.,* **37,** 2444–2457.

Li, L., G. Heymsfield, J. Carswell, D. Schaubert, M. McLinden, M. Vega, and M. Perrine, 2011: Development of the NASA High-Altitude Imaging Wind and Rain Airborne Profiler. *IEEE Aerospace Conference,* Big Sky, MT, Institute of Electrical and Electronics Engineers, 1–8, doi:10.1109/AERO.2011.5747415.

Lyons, W. A., and C. S. Keen, 1994: Observations of lightning in convective supercells within tropical storms and hurricanes. *Mon. Wea. Rev.,* **122,** 1897–1916.

MacGorman, D. R., and W. D. Rust, 1998: *The Electrical Nature of Storms.* Oxford University Press, 422 pp.

Mach, D. M., R. J. Blakeslee, M. G. Bateman, and J. C. Bailey, 2009: Electric fields, conductivity, and estimated currents from aircraft overflights of electrified clouds. *J. Geophys. Res.,* **114,** D10204, doi:10.1029/2008JD011495.

——, ——, ——, and ——, 2010: Comparisons of total currents based on storm location, polarity, and flash rates derived from high-altitude aircraft overflights. *J. Geophys. Res.,* **115,** D03201, doi:10.1029/2009JD012240.

Marks, F. D., Jr., and R. A. Houze Jr., 1987: Inner core structure of Hurricane Alicia from airborne Doppler radar observations. *J. Atmos. Sci.,* **44,** 1296–1317.

Molinari, J., P. K. Moore, V. P. Idone, R. W. Henderson, and A. B. Saljoughy, 1994: Cloud-to-ground lightning in Hurricane Andrew. *J. Geophys. Res.,* **99,** 16 665–16 676.

——, P. Moore, and V. Idone, 1999: Convective structure of hurricanes as revealed by lightning locations. *Mon. Wea. Rev.,* **127,** 520–534.

Naccarato, K. P., O. Pinto Jr., S. A. M. Garcia, M. Murphy, N. Demetriades, and J. Cramer, 2010: Validation of the new GLD360 dataset in Brazil: First results. Preprints, *International Lightning Detection Conference,* Orlando, FL, Vaisala, 6 pp. [Available online at http://www.vaisala.com/Vaisala%20Documents/Scientific%20papers/7.Naccarato,%20Pinto,%20Garcia.pdf.]

Petersen, W. A., S. A. Rutledge, and R. E. Orville, 1996: Cloud-to-ground lightning observations from TOGA COARE: Selected results and lightning location algorithms. *Mon. Wea. Rev.,* **124,** 602–620.

——, R. C. Cifelli, S. A. Rutledge, B. S. Ferrier, and B. F. Smull, 1999: Shipborne dual-Doppler operations and observations during TOGA COARE. *Bull. Amer. Meteor. Soc.,* **80,** 81–97.

Poelman, D. R., W. Schulz, and C. Vergeiner, 2013: Performance characteristics of distinct lightning detection networks covering Belgium. *J. Atmos. Oceanic Technol.,* **30,** 942–951.

Price, C., M. Asfur, and Y. Yair, 2009: Maximum hurricane intensity preceded by increase in lightning frequency. *Nat. Geosci.,* **2,** 329–332.

Rodger, C. J., S. Werner, J. B. Brundell, E. H. Lay, N. R. Thomson, R. H. Holzworth, and R. L. Dowden, 2006: Detection efficiency of the VLF World-Wide Lightning Location Network (WWLLN): Initial case study. *Ann. Geophys.,* **24,** 3197–3214.

Rogers, R. F., M. L. Black, S. S. Chen, and R. A. Black, 2007: An evaluation of microphysics fields from mesoscale model simulations of tropical cyclones. Part I: Comparisons with observations. *J. Atmos. Sci.,* **64,** 1811–1834.

Sadowy, G. A., A. C. Berkun, W. Chun, E. Im, and S. L. Durden, 2003: Development of an advanced airborne precipitation radar. *Microwave J.,* **46,** 84–98.

Samsury, C. E., and R. E. Orville, 1994: Cloud-to-ground lightning in tropical cyclones: A study of Hurricanes Hugo (1989) and Jerry (1989). *Mon. Wea. Rev.,* **122,** 1887–1896.

Saunders, C., 2008: Charge separation mechanisms in clouds. *Space Sci. Rev.,* **137,** 335–353.

——, and S. L. Peck, 1998: Laboratory studies of the influence of the rime accretion rate on charge transfer during crystal/graupel collisions. *J. Geophys. Res.,* **103,** 13 949–13 956.

Shao, X. M., and Coauthors, 2005: Katrina and Rita were lit up with lightning. *Eos, Trans. Amer. Geophys. Union,* **86,** 398.

Squires, K., and S. Businger, 2008: The morphology of eyewall lightning outbreaks in two category 5 hurricanes. *Mon. Wea. Rev.,* **136,** 1706–1726.

Stolzenburg, M., W. D. Rust, B. F. Stull, and T. C. Marshall, 1998: Electrical structure in thunderstorm convective regions: 1. Mesoscale convective systems. *J. Geophys. Res.,* **103** (D12), 14 059–14 078.

Szoke, E. J., E. J. Zipser, and D. P. Jorgensen, 1986: A radar study of convective cells in mesoscale systems in GATE. Part I: Vertical profile statistics and comparison with hurricanes. *J. Atmos. Sci.,* **43,** 182–197.

Takahashi, T., 1978: Riming electrification as a charge generation mechanism in thunderstorms. *J. Atmos. Sci.,* **35,** 1536–1548.

Tanelli, S., J. P. Meagher, S. L. Durden, and E. Im, 2004: Processing of high resolution, multiparametric radar data for the Airborne Dual-Frequency Precipitation Radar APR-2. Preprints, *Fourth Asia-Pacific Environmental Remote Sensing Symp.,* Honolulu, HI, SPIE, 5654-3.

Williams, E. R., 2009: The global electric circuit: A review. *Atmos. Res.,* **91,** 140–152, doi:10.1016/j.atmosres.2008.05.018.

——, and S. Stanfill, 2002: The physical origin of the land-ocean contrast in lightning activity. *C. R. Phys.,* **3,** 1277–1292.

Zipser, E. J., and K. R. Lutz, 1994: The vertical profile of radar reflectivity of convective cells: A strong indicator of storm intensity and lightning probability? *Mon. Wea. Rev.,* **122,** 1751–1759.